Materials
Horizons

ROYAL SOCIETY
OF CHEMISTRY

COMMUNICATION

View Article Online
View Journal | View Issue

Check for updates

Cite this: *Mater. Horiz.*, 2024, 11, 5786

Received 31st July 2024,
Accepted 11th September 2024

DOI: 10.1039/d4mh01007h

rsc.li/materials-horizons

# Autonomous humidity regulation by MOF/wood composites†

Kunkun Tu,‡[abc] Zhidong Zhang, ‡[d] Christopher H. Dreimol, [ce] Roman Günther,[f] Robert Zboray,[g] Tobias Keplinger, [ch] Ingo Burgert [ce] and Yong Ding *[ce]

**Maintaining indoor air relative humidity (R.H.) within the 40–60% range recommended by the American Society of Heating, Refrigerating, and Air-Conditioning Engineers (ASHRAE) significantly impacts human comfort and health. However, conventional solutions like dehumidifiers and humidifiers increase energy consumption, challenging the building sector's carbon neutrality goals. Here, we present an innovative composite material comprising wood and metal–organic frameworks (MOFs) that passively regulates indoor humidity by absorbing and releasing moisture. Our universal fabrication strategy enhances wood scaffold accessibility and increases MOF loading, resulting in a significant surface area increase, surpassing previous MOF/wood composites. This MOF/wood composite exhibits remarkable water sorption capacity, autonomously maintaining indoor humidity around 45% R.H. without external energy consumption. This aligns with ASHRAE recommendations, offering indirect energy savings and promoting a health-friendly indoor environment. Furthermore, the MOF/wood composite outperforms many existing materials in mechanical strength, dimensional stability, and scalability, making it highly suitable for building applications and contributing to carbon neutrality in the building sector.**

### New concepts

This work introduces a novel MOF/wood composite for passive indoor humidity regulation, maintaining relative humidity at around 45% without additional energy consumption. When triggered, the MOF/wood composite absorbs and releases moisture autonomously, offering an energy-efficient alternative to traditional dehumidifiers and humidifiers. The innovative fabrication method significantly increases the surface area of wood by loading MOFs, enhancing the material's performance. Distinct from existing research, our composite outstands in humidity regulation performance, mechanical strength, and dimensional stability. This study provides new insights into sustainable and smart building materials, highlighting their potential to create healthier indoor environments and contribute to energy conservation.

## Introduction

Relative humidity (R.H.) is crucial for both indoor comfort and human health. The American Society of Heating, Refrigerating, and Air-Conditioning Engineers (ASHRAE) has recommended maintaining an indoor R.H. range of 40–60% for optimal living conditions to minimize adverse health effects.[1,2] However, more than two-thirds of land areas experience humidity levels outside of the ideal humidity range and the outdoor climatic conditions have a significant effect on the indoor humidity variations.[3] Consequently, regulating systems are required to actively regulate indoor humidity to maintain a comfortable humidity range.[4–9] To date, the main solutions to actively control and tune indoor humidity are dehumidifiers and humidifiers. However, these energy-intensive devices cannot meet the current challenges of energy savings and carbon neutrality. Hence, autonomous humidity regulation systems that allow the humidity to be passively regulated through the exchange of moisture between hygroscopic materials and the surrounding environment have gained increasing attention.[10–16] Developing next-generation building materials that can automatically and simultaneously regulate indoor humidity would have remarkable potential in reducing the energy consumption of buildings and creating comfortable and healthy living conditions.

---

[a] *Jiangsu Key Laboratory of Coal-based Greenhouse Gas Control and Utilization, China University of Mining and Technology, Xuzhou, Jiangsu, 221008, China*
[b] *Carbon Neutrality Institute, China University of Mining and Technology, Xuzhou, Jiangsu, 221008, China*
[c] *Wood Materials Science, Institute for Building Materials, ETH Zürich, 8093, Zürich, Switzerland. E-mail: yoding@ethz.ch*
[d] *Durability of Engineering Materials, Institute for Building Materials, ETH Zurich, 8093 Zurich, Switzerland*
[e] *WoodTec Group, Cellulose & Wood Materials, Empa, 8600 Dübendorf, Switzerland*
[f] *Laboratory of Adhesives and Polymer Materials, Institute of Materials and Process Engineering, Zurich University of Applied Sciences, 8401 Winterthur, Switzerland*
[g] *Center for X-ray Analytics, Empa, 8600 Dübendorf, Switzerland*
[h] *AgroBiogel, 3430 Tulln, Austria*

† Electronic supplementary information (ESI) available. See DOI: **https://doi.org/10.1039/d4mh01007h**

‡ These authors contributed equally.

Wood is a carbon-storing and renewable building material with natural hygroscopicity because of its porous structure and lignocellulosic composition. Wood has been proven to be effective in mitigating R.H. changes by exchanging moisture with air.[17–21] However, the effectiveness of native wood in regulating humidity is limited by a comparably low sorption capacity and a slow rate of moisture exchange.[21] Moreover, the hygroscopic nature of wood causes fluctuations not only in its moisture content, but also results in poor dimensional stability due to shrinkage and swelling, which is often regarded as a flaw in practical applications.[22] Numerous efforts have been taken to improve the dimensional stability by wood modifications.[23–26] However, these modification methods usually further reduce the ability of wood to regulate humidity. Therefore, developing modification strategies that can improve the humidity regulation ability of wood while maintaining its dimensional stability is a key challenge.

One possible strategy is functionalization of wood with hygroscopic adsorbents. Previous work by Ran *et al.* introduced a deep eutectic solvent (DES) modified wood integrated with heat treatment.[27] The hygroscopic nature of DES combined with the increased porosity resulting from DES modification endowed the wood with an enhanced water sorption capacity. Ding *et al.* demonstrated that $CaCl_2$ modified wood shows effective indoor humidity regulation performance and was able to buffer a R.H. fluctuation of 75–30% to 51–34%.[28] However, the humidity regulation range with $CaCl_2$ modified wood does not coincide with the ideal humidity range for health promotion. Alternative adsorbents include silica gel, microporous zeolites, and molecular sieves.[29] Nevertheless, the practical application of these materials is limited by their high regeneration temperature or nonideal effective humidity range. In recent years, metal–organic framework materials (MOFs) have attracted increasing attention due to their remarkable potential in passive dehumidification and autonomous indoor humidity regulation, which is primarily attributed to their exceptional water vapor adsorption and storage properties.[30–38] To address the processing and handling challenges associated with the inherent nature of MOFs, strategies of incorporating MOFs within wood to build MOF/wood composites were developed.[39,40] By taking advantage of the good mechanical strength and the multi-scale porosity of wood, MOF/wood composites have been explored for various potential applications, such as gas separation,[39] water purification,[41] hydrogen generation,[40] energy harvesting[42] and *etc.* To date, the application of MOF/wood composites in the field of indoor humidity control has not been reported. Arguably, this is due to low MOF loading and an inhomogeneous MOF distribution in MOF/wood composites, mainly because of a restricted accessibility of the porous wood scaffold. Overcoming this challenge is crucial to achieve desirable humidity regulation performance.

In this work, we present a universal strategy for fabricating MOF/wood composites by enhancing the accessibility of porous wood through a laser-drilling process, followed by a multi-time MOF impregnation. The obtained MOF/wood composites showed remarkably high MOF loading and surface area, resulting in enhanced water sorption capacity. This composite can autonomously regulate indoor humidity by absorbing/releasing moisture, thereby maintaining the indoor humidity at ∼45% R.H. with near-zero energy consumption.

## Results and discussion

### Fabrication of MOF/wood composite

The porous structure of wood provides a suitable scaffold for hosting MOF particles, thereby addressing the challenges associated with processibility. However, the loading of MOFs is constrained by the limited accessibility of the porous structure of wood. Wood exhibits a distinctive hierarchical porous structure, characterized by hollow tube-like cells that are axially aligned (Fig. 1A). In this study, the focus was on the utilization of poplar wood with an axial tissue comprising vessels and fibers, with lumina diameters between 60–100 μm and 5–15 μm, respectively (Fig. 1B and C). Individual vessels are connected *via* pits, which facilitate water transport between vessels in the living tree. However, these water pathways restrict the passage of nanoparticles to deeper areas of the wood, which impedes a high loading of larger bulk wood specimens with MOFs, restricting their impact on the performance of the composite. In previous studies, pretreatment methods including delignification or carbonization have been primarily employed to enhance the accessibility of wood and thereby improve the MOF loading within MOF/wood composites (Table S1, ESI†).[39,43–51] However, these approaches often compromise the mechanical properties of wood. In contrast, the objective of this study was to preserve the natural properties of wood, including its appearance, structure, and mechanical strength, to the greatest extent. This challenge was addressed through a scalable two-step fabrication process (Fig. 1A). In the first step, we employed a laser drilling process to cut open vessels and fibers, resulting in so-called lasered wood (Fig. 1D and E and Movie S1, ESI†). The diameter of laser-drilled channels was approximately 300 μm with 100 μm distance between channels.

To find suitable MOFs for humidity regulation application, we compared the water adsorption capacity and desorption trigger points of commonly used MOFs and other representative water-adsorbing porous materials (Fig. S1, ESI†).[36,52–61] In this work, we selected MIL-101(Cr) to demonstrate proof of concept because of its widely reported high water sorption capacity and optimum regulation of moisture in the recommended R.H. range. These features reflect the working capacities and working humidity range to ensure an optimal humidity regulation performance. Studies on the toxicity of MIL-101(Cr), conducted both *in vitro*[62] and *in vivo*,[63] have demonstrated its biocompatibility. These findings suggest that MIL-101(Cr) can be safely used indoors without posing any health concerns.

In the next step, MIL-101(Cr) nanoparticles were synthesized and introduced into the wood scaffold to improve the water sorption capacity of wood. MIL-101(Cr) was successfully synthesized, and the morphology was studied by scanning electron microscope (SEM) (Fig. S2, ESI†). The crystalline structure was

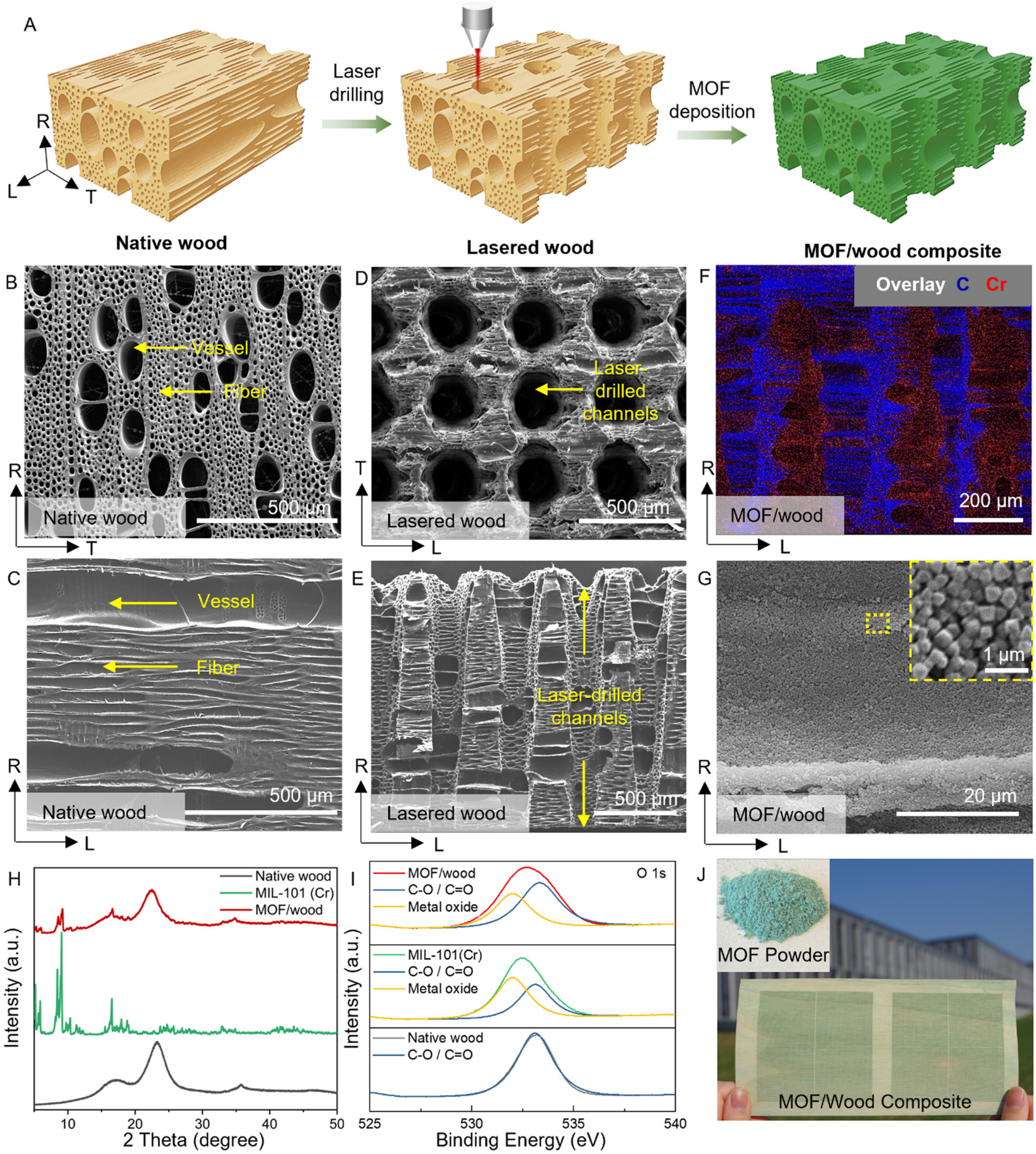

**Fig. 1** Fabrication of MOF/wood composite. (A) Illustrations of fabrication process and microstructure of MOF/wood composite. (R × L × T represents Radial × Longitudinal × Tangential directions). (B) Cross-sectional SEM image of native wood sample. (C) Radial-sectional SEM image of native wood sample. (D) Tangential-sectional SEM image of laser-drilled wood sample. (E) Radial-sectional SEM image of laser-drilled wood sample showing the wood fibers/vessels cut open. (F) EDXS mapping image of MOF/wood composite from radial-section showing the uniform distribution of MIL-101(Cr) on lasered-drilled wood scaffold. (G) Radial-sectional SEM image of MOF/wood composite with uniform MOF coating on the lumen surface. (H) XRD spectra of native wood, MIL-101(Cr) and MOF/wood composite. (I) XPS spectra of the O 1s peak of native wood, MIL-101(Cr) and MOF/wood composite. (J) An image of the MIL-101(Cr) powder and MOF/wood composite.

confirmed by X-ray diffraction (XRD) measurements (Fig. 1H). Water sorption isotherms of the as-synthesis MIL-101(Cr) showed high water uptake capacity of 142%, together with a steep S-shaped sorption isotherm (Fig. S3, ESI†). The pronounced sorption hysteresis happened at ∼40% R.H., falling into the ideal humidity range.

After synthesis, MIL-101(Cr) MOFs were introduced into the wood scaffold *via* an *ex situ* growth approach. The *ex situ* growth method is beneficial for achieving high and controllable MOF loading by regulating the impregnation time. SEM and energy-dispersive X-ray spectroscopy (EDXS) mapping demonstrated that after 15 impregnation cycles, a dense layer of MOF is deposited on the wood cell wall (Fig. 1F and G and Fig. S4, ESI†), as confirmed by respective XRD patterns and X-ray photoelectron spectroscopy (XPS) spectra peaks (Fig. 1H and I). The organic ligand employed in the synthesis of MIL-101(Cr) is terephthalic acid ($C_8H_6O_4$), which contains numerous carboxyl groups, capable of forming hydrogen bonds with the hydroxyl groups present on the wood surface, thereby facilitating the anchoring of MIL-101(Cr) on the wood surface. Consequently, MIL-101(Cr) can demonstrate consistent and robust adhesion to inner walls of wood cells, thereby mitigating concerns related to MOF aggregation, uneven distribution, and weak interaction.

Compared to one impregnation cycle that results in a MOF loading of approximately 1%, the MOF loading can reach up to 17% after 15 impregnation cycles. Multi-time coating strategy allows to achieve a high loading efficiency of MOF (Fig. 2A and B, and Fig. S5, ESI†). It is worth mentioning that the multi-time coating strategy is only feasible for lasered wood as its porosity is easily accessible after opening the wood fibers with laser. After 15 immersing cycles, the MOF loading of non-lasered wood is only around 2%, proving the necessity of the laser drilling process (Fig. 2B and C). In addition to penetration through the open cells from the cross section of wood, MOFs are able to access the wood structure through the laser drilled channels. Wood membranes with a thickness from 0.8 mm to 4 mm showed similar MOF loading after 15 impregnation cycles (Fig. 2D).

The high loading of MOF significantly affects the porosity, which was studied by $N_2$ sorption (Fig. 2E and Fig. S6 and S7, ESI†). The $N_2$ adsorption isotherms of native wood revealed low surface area whereas the resulting MOF/wood composite exhibited remarkably improved surface area because of the incorporation of MOFs. While native wood showed a

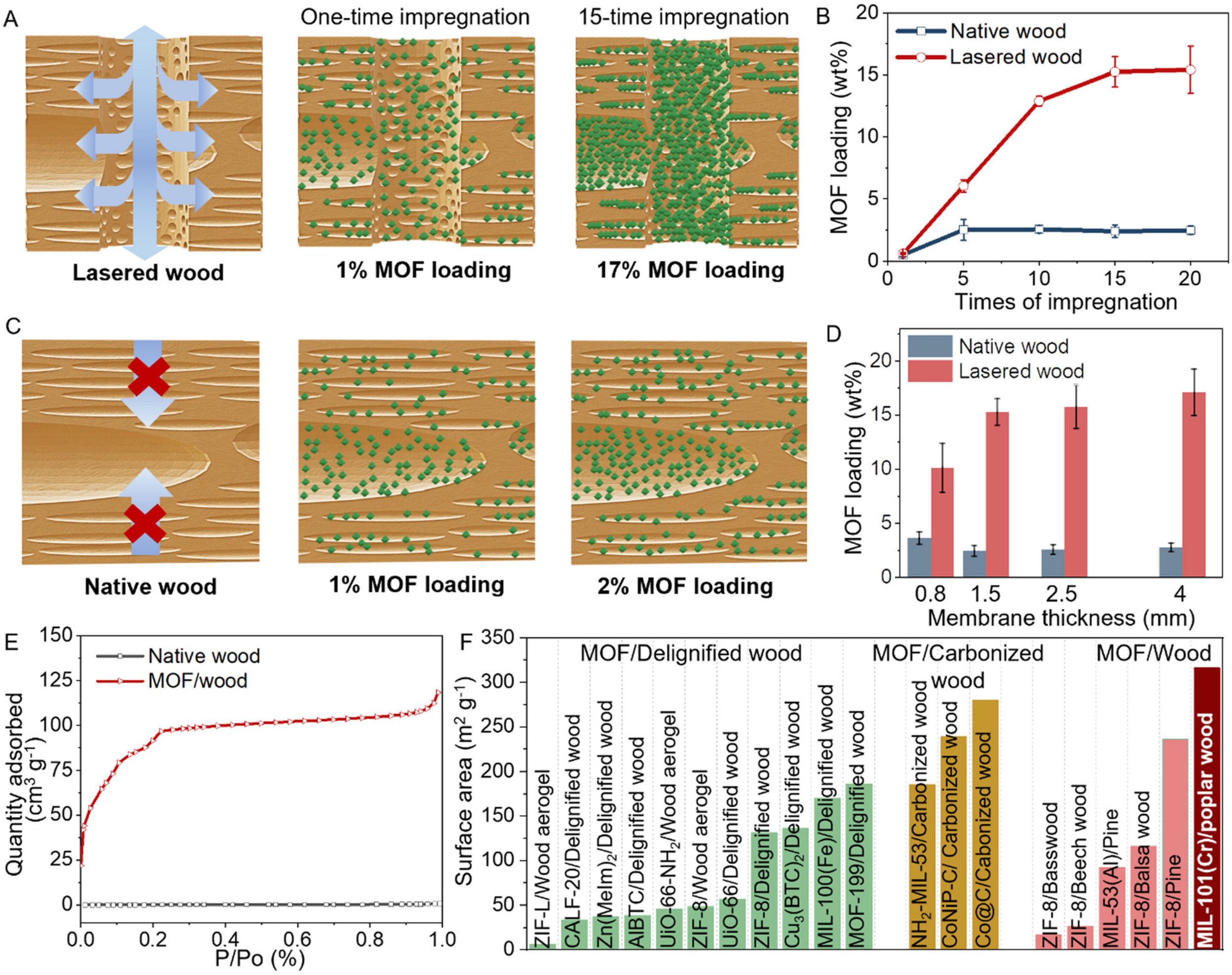

Fig. 2 The impact of preparation parameters on the MOF loading. (A) Schematic representation of the MOF loading state on lasered wood cell wall after one time and 15-time coating. (B) MOF loading on native wood scaffold and lasered wood scaffold with varying impregnation times. (C) Schematic representation of the MOF loading state on native wood cell wall after one time and 15-time coating. (D) The MOF loading on native wood scaffold and lasered wood scaffold with varying membrane thickness after 15 impregnation cycles. (E) $N_2$ adsorption isotherms of native wood and MOF/wood composites. (F) BET surface area calculated from $N_2$ adsorption and comparison with previous works.

Brunauer–Emmett–Teller (BET) surface area of 0.343 $m^2\ g^{-1}$, the pure MIL-101(Cr) showed a BET surface area of 2791 $m^2\ g^{-1}$ (Table S2, ESI†), resulting in MOF/wood composite with a BET surface area of 316 $m^2\ g^{-1}$, which was 920 times increased compared to native wood. The surface area of the MOF/wood composite developed in this work surpasses previously reported MOF-modified wood composites, due to the high loading of MOFs (Fig. 2F and Table S1, ESI†).[43–51,64–66]

## Investigation of water sorption and dimensional stability

We further investigated the water sorption capacity of native wood and the MOF/wood composite with a dynamic vapor sorption (DVS) analyzer. The water sorption capacities of native wood and the MOF/wood composite are 28.35% and 39.42%, respectively. The enhanced water uptake capacity of the MOF/wood composite is attributed to its high surface area and hygroscopic properties, which result from the substantial MOF loading (Fig. 3A and Fig. S8, ESI†). Notably, the MOF/wood composite also exhibits a more suitable sorption/desorption humidity range compared to native wood. At around 40% R.H., the composite demonstrates the highest hysteresis, which is advantageous for humidity regulation (Fig. 3B). After a ten-cycle measurement, the sample revealed no decrease in water sorption capacity, indicating stable composite-water interactions (Fig. 3C). Overall, the MOF/wood composite developed in this work successfully met the criteria for humidity regulation application: (1) high water-uptake capacity, (2) steep S-shaped sorption isotherms with a pronounced hysteresis in the ASHRAE requisite range of 40–60% R.H., and (3) long-term stability and cycling performance.

Dimensional stability under dynamic humidity levels is another crucial factor for the applicability of the composites. An increase in moisture content of wood results in swelling, which varies in magnitude along different directions, owing to the anisotropic structure of wood. Native poplar wood showed a maximum swelling of 8.2% in the tangential direction, 3.2% in the radial direction, and 0.27% in the longitudinal direction, when exposing oven-dry samples to 95% R.H. Even though the MOF/wood composite exhibited enhanced water absorption capacity due to the incorporation of MOFs, they still maintained much better dimensional stability than the native wood (Fig. 3D). MOF/wood composite showed less pronounced swelling, ~3.2% in the tangential direction, ~2.0% in the radial direction, and ~0.22% in the longitudinal direction. Even after 100 wetting/drying cycles, no cracking or bending of the MOF/wood samples was observed (Fig. 3E). Besides long-term stability and dimensional stability, the mechanical properties of the composites also play an important role in their usage, particularly in building scenarios. After laser drilling, the lasered wood showed an ultimate tensile stress of ~24 MPa, which is 40% less compared to native wood, but still provides sufficient mechanical stability. The ultimate tensile stress of MOF/wood composite remained comparable to that of lasered wood, suggesting that the MOF coating process did not further alter the mechanical properties of the composite (Fig. 3F and Table S3, ESI†).

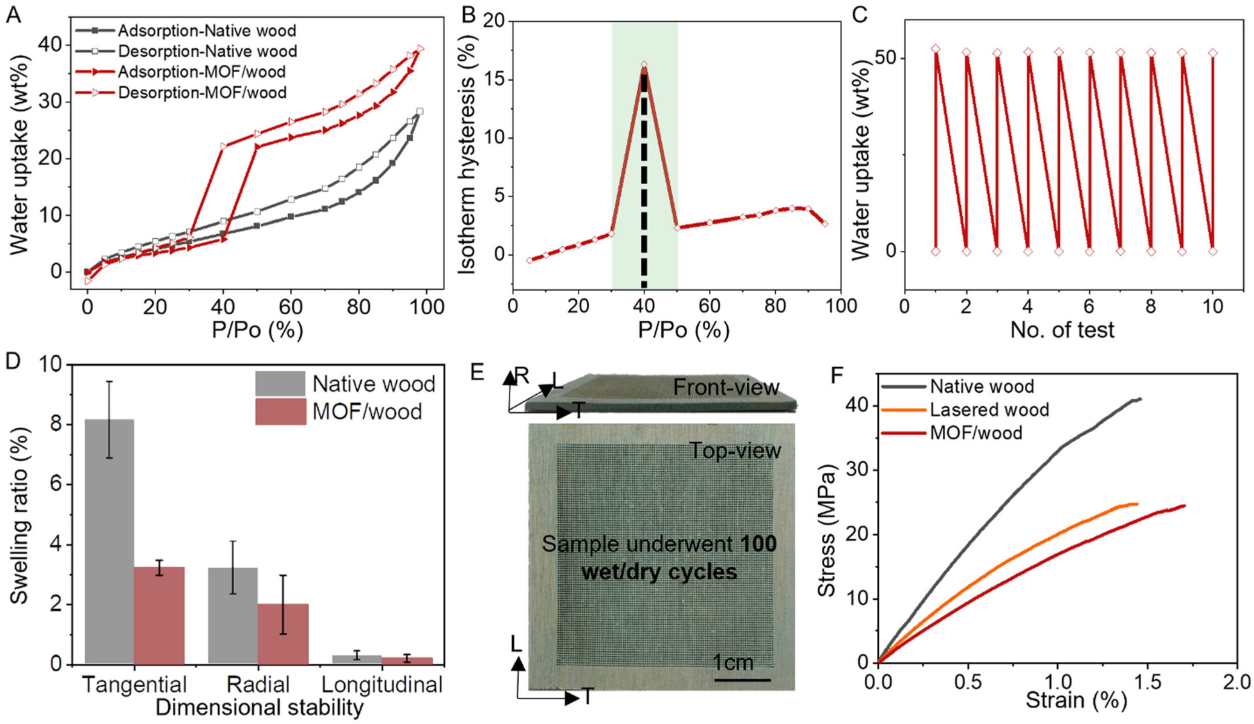

Fig. 3 Water vapor sorption-desorption performance and dimensional stability. (A) Water sorption isotherms. (B) Water sorption hysteresis isotherms. (C) Water sorption cyclic tests of MOF/wood composite. (D) The swelling of oven-dry native wood and MOF/wood composite after exposure to 95% R.H. for 24 hours. (E) Images of MOF/wood samples after 100 wet/dry cycles. (F) Strain-stress diagrams from tensile tests.

### Humidity regulation performance

The enhanced water sorption performance and dimensional stability indicate the composite's potential for passive humidity regulation. The humidity regulation performance was further investigated with experiments and simulations. We constructed a test chamber, equipped with four sample "windows", humidity sensors, and a data recording unit (Fig. 4A and Fig. S9, ESI†). The humidity inside the test chamber was considered as 'indoor humidity'. The test chamber was positioned in a climate chamber to ensure precise control of the external humidity or ambient humidity. The experimental conditions simulated a humidity change from a humid stage to a dry stage. The ambient temperature was kept constant at 23 °C, and the ambient humidity initially set at 70% R.H. for 8 hours to simulate a humid environment. Subsequently, the humidity was changed to 25% R.H. for another 16 hours to simulate a dry environment. The testing conditions and time scale were selected to mimic realistic conditions with longer daytime and short nighttime.

By subjecting the test chamber to dynamic humidity changes, one can test the capability of hygroscopic materials to autonomously regulate humidity by reversible moisture absorption/desorption. Humidity fluctuation is a necessity to trigger the moisture exchange between the materials and ambient. In this work, we studied the humidity regulation performance of native wood and MOF/wood composite. The effective humidity regulation relies in the capture/storage of water vapor at relatively high R.H. level (water absorption stage) and subsequently release of moisture at relatively low R.H. level (water desorption stage). As discussed before, the S-shaped sorption isotherms with adequate hysteresis loop indicate the effective working range, capacity and efficiency. When the ambient R.H. swung from 70% to 25%, the indoor humidity with native wood windows fluctuated together with the ambient humidity because the natural porosity of wood allows for the moisture exchange. Due to the limited water sorption, native wood is not capable of passively regulating indoor humidity by

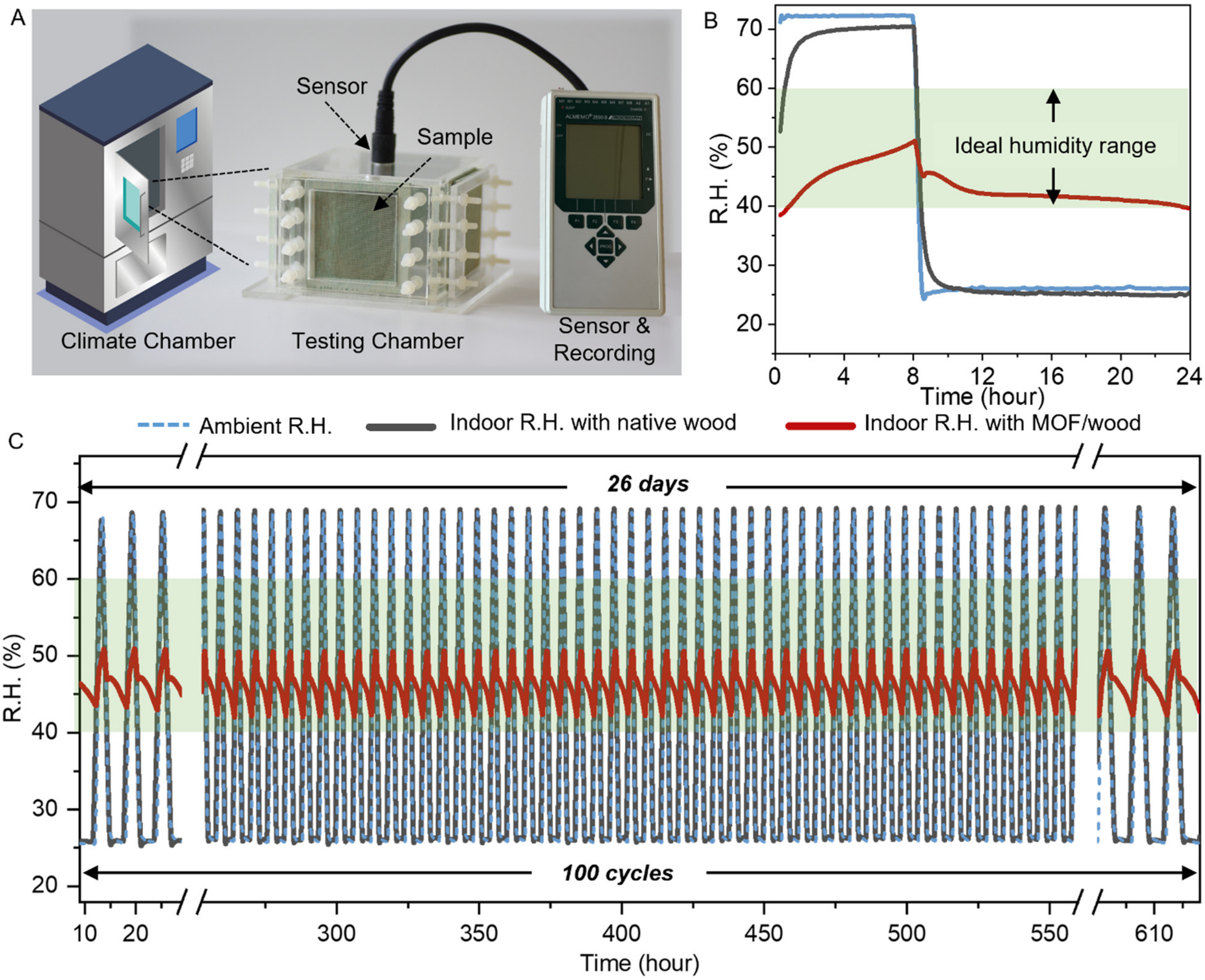

Fig. 4 Humidity regulation performance and long-term stability. (A) Setup for indoor humidity regulation measurement, including house model with mounted samples, humidity sensors, data recording units. The testing chamber was put in a climate chamber to control ambient humidity and temperature. (B) Indoor humidity curves resulting from dynamic climate condition changes (70% R.H., 8 hours; 25% R.H., 16 hours). (C) 100 cycles (26 days) of the humidity regulation performance test using MOF/wood composite.

water sorption/desorption effectively, leading to a large fluctuation range of indoor R.H. Therefore, native wood showed minimal humidity buffering capacity, which resulted in indoor humidity falling outside the ideal humidity range (Fig. 4B).

In contrast, the MOF/wood composite windows were able to store moisture to fully mitigate the humidity increase and stabilized the humidity precisely in the range of 40–50% in the 8 hours of increased humidity (*e.g.*, at nighttime). When the ambient humidity dropped to 25%, the MOF/wood composite released moisture and maintained the indoor humidity in the range of 40–50% (*e.g.* at daytime). The humidity regulation performance of MOF/wood composite was able to counterbalance the humidity fluctuation in the time range of 24 hours, demonstrating great potential for buffering real-world humidity fluctuations. Moreover, the indoor humidity range was precisely regulated in the range of 40–50% (ideal humidity level for health). Due the mild regeneration conditions of MIL-101(Cr), the humidity balancing happened autonomously, without the need for additional energy input during operation. The effectiveness of humidity regulation is determined by the capability of the MOF/wood composite to absorb/desorb moisture in an effective humidity working range.

The practical utilization for indoor humidity control depends on the long-term stability of the MOF/wood composite. Therefore, we further measured its stability of humidity regulation performance by means of cyclic tests. The ambient humidity changed from 70% to 25% in 100 cycles. The MOF/wood composite were able to maintain the indoor R.H. between 40% and 50%, inhibiting high humidity fluctuations and favoring living comfort (Fig. 4C). Humidity regulation performance exhibited no decline over 100 cycles (26 days), highlighting the remarkable stability and durability of the MOF/wood composite. This underscores its significant potential for practical application in real world scenarios.

We further carried out numerical simulations to understand the moisture transport through wood and its influence on relative humidity regulation when the R.H. changes from 20% to 70%. (Fig. 5). For these simulations, several assumptions were made to simplify the model implementation (see Methods for more details). Notably, simulations were not conducted at the same scale or with the same geometry as the experiment. Numerical simulations were performed at the microscopic scale assuming all lasered holes are identical (Fig. S10, ESI†). Although this microscopic level simulation domain cannot fully

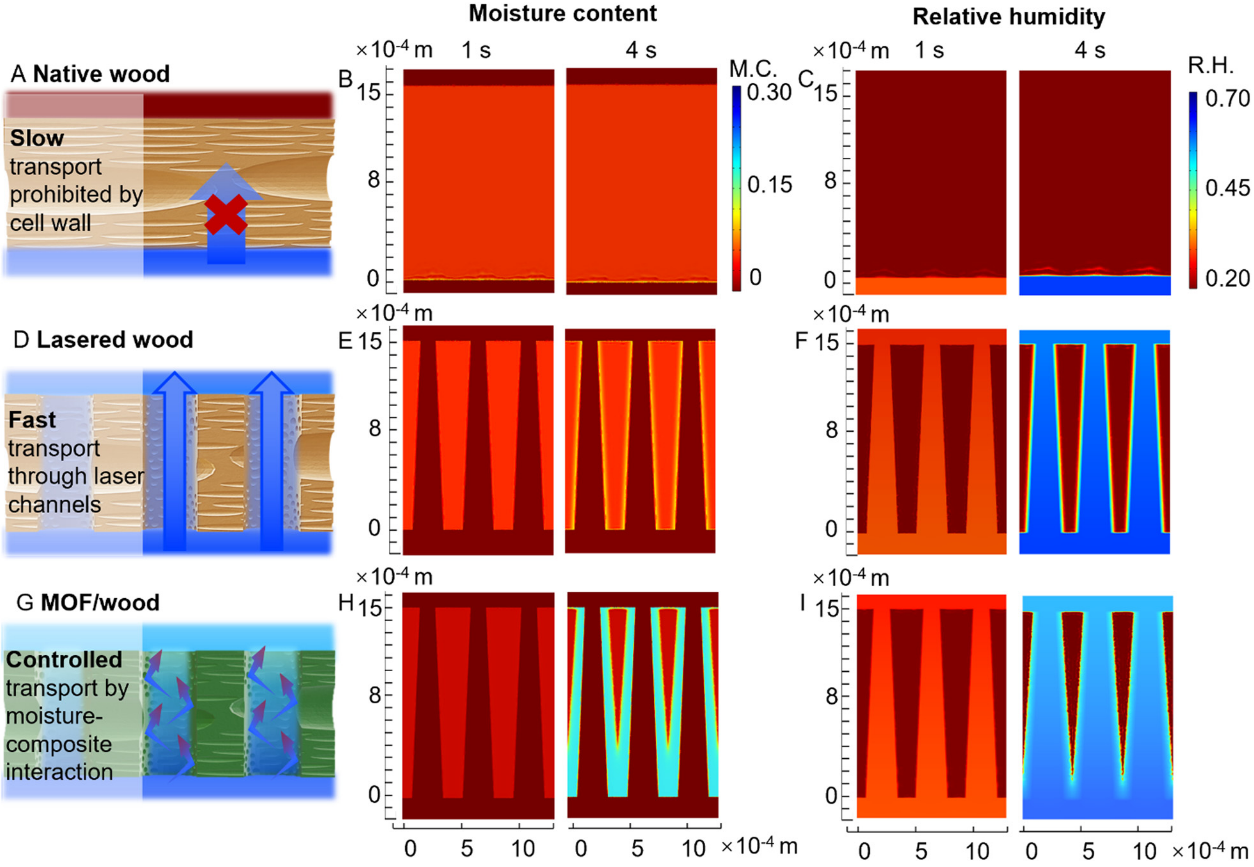

Fig. 5 Simulation of moisture content (M.C.) distribution within native wood, lasered wood, and MOF/wood composite and its influence on R.H. (A, D, G) Illustrations of simulation boundary and moisture transfer of native wood, lasered wood, and MOF/wood composite, respectively. (B, E, H) Simulated M.C. distribution during moisture transport for native wood, lasered wood, and MOF/wood composite, respectively. Moisture transport through the thin wood materials with an initial R.H. of 20% and an external R.H. of 70%. (C, F, I) Influence on R.H. evolution for native wood, lasered wood, and MOF/wood composite, respectively.

represent the experimental results at macroscopic scale, these simulation results aim to illustrate their abilities on humidity regulation.

Moisture transport through a wood sample is influenced by water permeability, vapor diffusion coefficient, and moisture retention capacity (Fig. S11, ESI†). Moisture diffusion through solid wood is typically slow because of its dense cell wall structure (Fig. 5A–C). However, the diffusion of moisture is accelerated after laser drilling as this process opens up the cell structure (Fig. 5D–F). The water vapor sorption isotherm showed that the MOF/wood composite exhibited the highest water sorption hysteresis at 40% R.H. This resulted in a significant alteration in the moisture content of the composite once the ambient humidity reached 40% R.H., leading to a substantial change in moisture content within this specific R.H. range (Fig. 5G and H). The MOF/wood composites can slow down the moisture diffusion through the material by absorbing water (Fig. 5I). The simulation results clearly demonstrate that the MOF/wood composite exhibits superior humidity regulation capabilities compared to both native and lasered wood.

### Application scenarios

Global humidity distribution reveals the great range of humidity levels in different geological regions (Fig. 6A). The diurnal humidity fluctuations add to the complexity of the problem (Fig. 6B). Despite differences in building characteristics and climate control, outdoor weather conditions have an influence

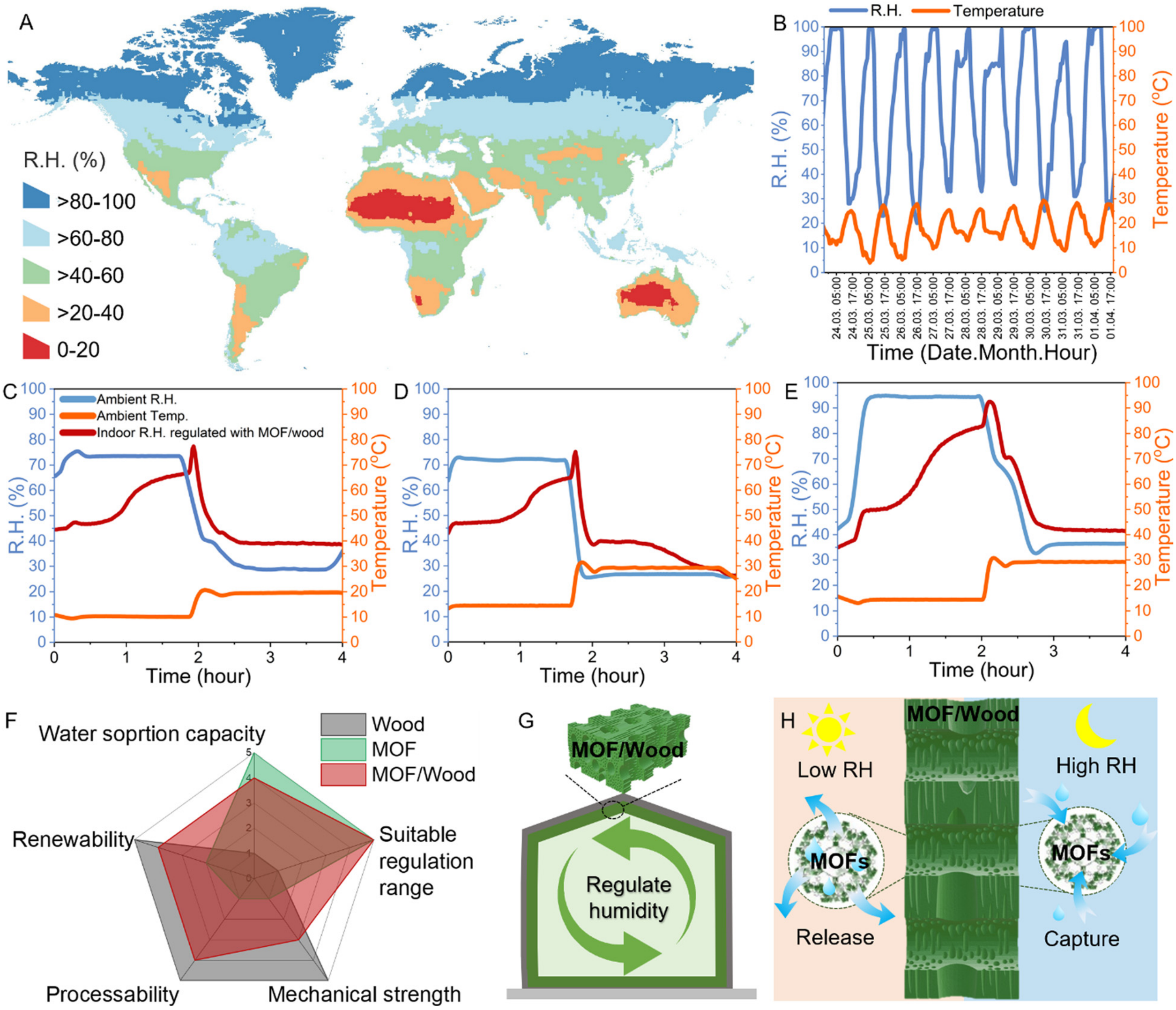

Fig. 6 Application scenarios of MOF/wood composite. (A) Global average annual humidity map showing that humidity levels in most land areas fall outside of the ideal humidity range. (B) Representative diurnal humidity and temperature fluctuations. Data source: weather station Canberra (airport), Australia during the period of March 24th to April 1st, 2024. (C)–(E) Humidity regulation performance of MOF/wood composite under various climate types. (C) Condition 1: Ads. 10 °C, 75%R.H., Des. 20 °C, 25%R.H. (D) Condition 2: Ads. 15 °C, 75%R.H., Des. 30 °C, 25%R.H. (E) Condition 3: Ads. 15 °C, 95%R.H., Des. 30 °C, 35%R.H. (F) Radar plots showing the performance of native wood, pure MOF and MOF/wood composite. (G) Scheme showing the application scenario of MOF/wood composite in passive humidity regulation. (H) Mechanism of the proposed passive humidity regulation strategy that generated by the water exchange between MOF/wood composite and surrounding air.

on the indoor climate, meaning outdoor and indoor humidities are closely correlated.[3,67–69] Since people spend nearly 80–90% of their time indoors nowadays, indoor climate needs to be actively controlled to be in a narrower range compared to outdoors. Consistent and adjusted indoor humidity benefits living comfort and health conditions.[4]

Instead of working against these natural diurnal humidity fluctuations with energy input, these humidity fluctuations can be utilized in the autonomous regulation approach. Autonomous humidity regulation requires dynamic humidity levels as triggers to the exchange of moisture between hygroscopic materials and ambient, resulting in the buffering effect of fluctuations. To study the humidity regulation potential with MOF/wood composite under various climate types, we conducted tests under three distinct conditions characterized by high variability of R.H. and temperature: (i) adsorption (Ads.) at 10 °C, 75%R.H., and desorption (Des.) at 20 °C, 25%R.H. (Fig. 6C); (ii) Ads. at 15 °C, 75%R.H., and Des. at 30 °C, 25%R.H (Fig. 6D); (iii) Ads. at 15 °C, 95%R.H., and Des. at 30 °C, 35%R.H. (Fig. 6E). Results showed that our MOF/wood composites effectively reduce the indoor humidity fluctuation and exhibit a strong humidity buffering effect even under various extreme conditions. These findings have great practical relevance in terms of the composites' universal compatibility with various climate types.

The well-balanced performance of MOF/wood composites in terms of humidity regulation potential and materials integrity, makes them suitable to be embedded into buildings for autonomous humidity regulation (Fig. 6F). We envisage that MOF/wood composites have the capability to decrease indoor humidity through water adsorption during humid nighttime, while increasing moisture in the indoor air through water desorption during dry daytimes (Fig. 6G and H). Instead of consuming energy and requiring complicated facilities to work against the diurnal humidity fluctuations, the proposed passive regulation strategy works together with these dynamic conditions with the inherent properties of the MOF/wood composite. This buffering effect could reduce the amplitude of diurnal humidity fluctuations and thus lead to indirect energy savings for maintaining indoor humidity and improve living comfort. This is especially important to rural areas and climate harsh regions where buildings are poorly climate insulated and lacks energy and resources for active humidity control facilities. It is noteworthy that the passive regulation approach may be less effective for climate types where the relative humidity is constantly low or high.

## Conclusions

In summary, this study examined an autonomous humidity regulation MOF/wood composite. The composite was created using a universal fabrication strategy that overcomes the insufficient diffusion of the MOF nanoparticles into the inner regions of wood panels. This strategy ensures a high MOF loading of 17% and a high surface area of 316 $m^2\ g^{-1}$, which was 920 times higher than that of native wood, surpassing previously reported MOF/wood composites. The water adsorption and desorption abilities, the 3D moisture transport process and the indoor humidity regulation performance of the MOF/wood composites were systematically investigated. It was found that the obtained MOF/wood composite showed excellent water sorption capacity, an ideal working humidity range of 40–60% R.H., and long-term stability and cycling performance. Moreover, the MOF/wood composite exhibited sufficient mechanical strength and improved dimensional stability. It demonstrated the ability to regulate indoor humidity autonomously within the range recommended by ASHRAE, which is highly advantageous for indirect energy saving and maintaining a health-friendly indoor climate. These characteristics make it highly suitable for use in building scenarios and open the venues for the development of a new generation ventilation systems.

## Experimental

### Synthesis of MIL-101(Cr)

For a typical synthesis process, 150 mL sodium acetate ($C_2H_3NaO_2$, ≥99.0% purity) aqueous solution was prepared with a concentration of 0.05 mol $L^{-1}$. Then 4.95 g (0.03 mol) terephthalic acid ($C_6H_4(CO_2H)_2$) and 12 g chromium nitrate ($Cr(NO_3)_3$) was added in the last solution in turn. The mixed solution was transferred to an autoclave and then placed in an oven with 200 °C for a reaction period of 20 h. After slowly cooling to ambient temperature, the synthesized MIL-101(Cr) was collected through repeated centrifugation and thoroughly washed twice with dimethylformamide (DMF), twice with ethanal, and twice with water. The obtained products were then dried at 120 °C in vacuum oven.[70,71]

### Laser drilling processing of wood

Poplar wood (*Populus tremula*) tangential sections with the dimension of 50 mm × 50 mm × 1.5 mm ($L \times T \times R$) were cut. $T \times L \times R$ represents tangential × longitudinal × radial directions were cut with a circular saw. A commercial 10.6 μm $CO_2$ laser engraver (Speedy 300, Trotec) was used to produce the lasered wood with the desired pattern. The power of the laser beam is 20 W, the scan rate is 2.5 mm $s^{-1}$, and the image density is 1000 pulses per inch. The defocus distance is zero.[28]

### Fabrication of MOF/wood composite

MIL-101(Cr) powder was dispersed in ethanol solution to obtain a MOF solution with a concentration of 10 g $L^{-1}$. In a subsequent step, the lasered wood samples were impregnated in the MOF solution for 12 h at room temperature under gentle stirring. The composite was then dried at 103 °C for 12 h. This is a typical procedure of one impregnation cycle. This impregnation process was repeated in cycles, namely multi-times impregnation.

### Material characterization

X-ray powder diffraction (Panalytical X'Pert PRO MPD) was performed using Cu Kα radiation ($\lambda$ = 1.5406 Å). The diffractometer was operating at 40 kV and 45 mA with an angular step size of 0.03° and a counting time of 1 s per step. XPS was performed using a Physical Electronics Quantera SXM spectrometer using monochromatic Al Kα radiation generated from an electron beam operated at 15 kV and 49.3 W. The spectra were collected under ultrahigh vacuum conditions (residual pressure $\approx 1 \times 10^{-6}$ Pa) at a pass energy of 55.0 eV. The morphology and element composition of the samples were characterized using a SEM (FEI Quanta 200F, Hillsboro, OR, USA) equipped with EDXS (Ametek-EDAX). A Pt–Pd (80/20) coating of ~10 nm thickness was applied to the samples with a sputter coater (CCU-010, Safematic, Switzerland). X-ray microtomography was performed with an EasyTom XL Ultra 230–160 device (RX Solutions, France) at an acceleration voltage of 95 kV. Images were collected with a flat panel detector. Nitrogen adsorption was conducted using an ASAP 2010 apparatus from Micromeritics. About 0.5 g samples were degassed with the pressure level at 5 μm Hg and temperature at 60 °C. Tensile tests were performed using a universal testing machine (Zwick Roell) equipped with a 10 kN load cell. Ten specimens of each sample stored at 20 °C and 65% relative humidity with the dimensions $5 \times 50 \times 1.5$ mm$^3$ (tangential × longitudinal × radial) were tested in longitudinal direction with a span length of 25 mm. The testing speed was 0.5 mm min$^{-1}$.

### Water vapor sorption isotherms

Dynamic water vapor adsorption and desorption was measured by an automated sorption balance device (DVS Advantage ET85, Surface Measurement Systems Ltd). Ten milligrams of each sample were first dried for 10 h at 60 °C and at a partial water vapor pressure of $p/p_0 = 0$. The measurement was carried out with ascending $p/p_0$ steps of 0, 0.05, 0.10, 0.15, 0.20, 0.25, 0.30, 0.40, 0.60, 0.80, 0.85, 0.90, 0.95, and 0.98 for adsorption and then with descending steps in the same manner for desorption at 25 °C. Equilibrium in each step was defined to be reached at a mass change per time (d$m$/d$t$) of less than 0.0005%/min over a 10 min window or a maximal time of 1000 min per step. The samples were exposed to a flow rate of 200 sccm, and the carrier gas used was $N_2$.

### Water vapor sorption cyclic test

To measure the water vapor sorption performance of transpiring wood in a time-wise manner, we carried out 10 cycles of measurements. One transpiring wood sample about ten milligrams was first dried for 10 h at 60 °C. Two treatment steps were then performed: $p/p_0$ 0.98 at 20 °C, $p/p_0 = 0$ at 40 °C. Equilibrium in each step was defined to be reached at a mass changer per time (d$m$/d$t$) of less than 0.001% over a 10 min window or a maximum time of 720 min per step.

### Dimensional stability

For assessing the dimensional stability, native wood, laser drilled wood, and MOF/wood composites were oven-dried at 103 °C for 24 hours. Ten specimens of each sample were measured. The specimen size on tangential, radial, and longitudinal direction were recorded as $\alpha_{t,\text{dry}}$, $\alpha_{r,\text{dry}}$, $\alpha_{l,\text{dry}}$, respectively. The specimens were then conditioned at 23 °C at a R.H. of 95% for 24 hours. The specimen size on tangential, radial, and longitudinal direction were recorded as $\alpha_{t,\text{wet}}$, $\alpha_{r,\text{wet}}$, $\alpha_{l,\text{wet}}$, respectively. The swelling was calculated with eqn (1)–(3):

$$\text{Swelling}_{\text{tangential direction}} = (\alpha_{t,\text{wet}} - \alpha_{t,\text{dry}})/\alpha_{t,\text{dry}}\ [\%] \quad (1)$$

$$\text{Swelling}_{\text{radial direction}} = (\alpha_{r,\text{wet}} - \alpha_{r,\text{dry}})/\alpha_{r,\text{dry}}\ [\%] \quad (2)$$

$$\text{Swelling}_{\text{longitudinal direction}} = (\alpha_{l,\text{wet}} - \alpha_{l,\text{dry}})/\alpha_{l,\text{dry}}\ [\%] \quad (3)$$

### Humidity regulation test

The humidity regulation testing chamber is showed in Fig. S8 (ESI†). The testing chamber framework is made of plastic board with four openings, or "windows", to mount the samples. The size of the testing chamber was 7 cm × 7 cm × 5 cm (width× depth × height). The tested sample had a dimension of 5 cm × 5 cm × 0.15 cm ($L \times T \times R$). The test chamber was designed at a scale of 1 : 50 to a residual living room with a dimension of 3.5 m × 3.5 m × 2.5 m (width× depth × height). The volume ratio of sample/space was 0.061. Native wood and MOF/wood composites were mounted in the windows. The testing chamber was placed in a climate chamber, in which ambient temperature and humidity can be well-controlled (Fig. 4A). Humidity sensors were installed inside the testing chamber and climate chamber. When subjecting to different ambient humidity levels, the changes in indoor climate and sample surface temperature were recorded. Test conditions: Dynamic humidity condition was set to simulate the diurnal humidity change, that is humid nighttime and dry daytime. The ambient climate was controlled as: nighttime: 23 °C, 70% R.H., 8 hours; daytime: 23 °C, 25% R.H., 16 hours.

### Moisture transport simulations

For numerical simulations, the thickness of the wood samples was set as 1.5 mm. Native wood was set as an anisotropic homogenous porous material. We consider laser-drilled wood and MOF/wood composite to consist of two parts, wood phase and lasered holes. A continuum two-phase moisture transport model was employed to consider both liquid advection and vapor diffusion.[72] The size of the lasered holes and the ratio of the wood phase to the lasered hole phase were estimated from the SEM images in Fig. 1. Different moisture transport models were used for moisture transport in the wood phase and the lasered holes. The moisture transport coefficient of the wood phase was set to be 50 times higher for the longitudinal transport than the radial and tangential transport.[73] In lasered holes, only vapor diffusion driven by the gradient of R.H. was simulated.[74] Numerical simulations were performed on one lasered hole and its corresponding volume of wood as illustrated in Fig. S10 (ESI†). The initial R.H. of simulation domain (wood phase and lasered holes) and boundary condition (surroundings) was set at 20%. Then the boundary condition was changed to 70% R.H. to simulate the water adsorption process of samples and its influence on R.H. and moisture content in the simulation domain (see ESI† for more details).

## Author contributions

Y. D. proposed the project and conceived the idea. Y. D. supervised the project. Y. D. and K. T. designed the experiments. Y. D., Z. Z., C. D., R. Z., and K. T. carried out the experiments and analyzed the data. Y. D. and K. T. organized and wrote the manuscript. All authors contributed to the discussion and commented on the manuscript.

## Data availability

Further information and requests for data and resources will be fulfilled by the lead contact: Yong Ding.

## Conflicts of interest

The authors declare no competing interests.

## Acknowledgements

The project was conducted in the framework of the SNF project ''Hierarchical cellulose scaffolds for structural and functional gradient materials'' (200021_184821/1). K. T. was supported by the grants from the Science and technology project of Xuzhou (Grant No.KC23003), the Fundamental Research Funds for the Central Universities (No. 2024QN11068) and ''Double Innovation'' Doctor of Jiangsu Province (No. 140924007). We thank the Scientific Center for Optical and Electron Microscopy at ETH Zurich for providing access to their facilities and Thomas Schnider for the wood sample preparation.

## References

1 M. G. Qin, P. M. Hou, Z. M. Wu and J. T. Wang, *Build. Environ.*, 2020, **169**, 11.

2 A. ASHRAE, American Society of Heating, Refrigerating, and Air-Conditioning Engineers, Inc., Atlanta, GA, 2021.

3 J. L. Nguyen and D. W. Dockery, *Int. J. Biometeorol.*, 2016, **60**, 221–229.

4 A. V. Arundel, E. M. Sterling, J. H. Biggin and T. D. Sterling, *Environ. Health Perspect.*, 1986, **65**, 351–361.

5 M. Shehadi, *J. Build. Eng.*, 2018, **19**, 539–551.

6 P. Wolkoff, *Int. J. Hygiene Environ. Health Perspect.*, 2018, **221**, 376–390.

7 A. V. Arundel, E. M. Sterling, J. H. Biggin and T. D. Sterling, *Environ. Health Perspect.*, 1986, **65**, 351–361.

8 M. Posani, V. Vera, O. Pietro, C. Brumaud, B. Dillenburger and H. Guillaume, *Nat. Commun.*, 2023, DOI: 10.21203/rs.3.rs-3427939/v1.

9 D. Amaripadath, R. Rahif, M. Velickovic and S. Attia, *J. Build. Eng.*, 2023, **68**, 106039.

10 M. G. Qin, P. M. Hou, Z. M. Wu and J. T. Wang, *Build. Environ.*, 2020, **169**, 106581.

11 Z. M. Wu, M. H. Qin and M. J. Zhang, *Energy Build.*, 2018, **174**, 254–261.

12 M. Qin, 1st International Conference on Moisture in Buildings, 2021.

13 H. Xue, B. Chen and Y. Wang, *Langmuir*, 2024, **40**, 12810–12817.

14 A. Entezari, H. Lin, O. C. Esan, W. Luo, R. Wang, R. You and L. An, *Cell Rep. Phys. Sci.*, 2023, **4**, 101278.

15 Y. Lin, K. Shao, S. Li, N. Li, S. Wang, X. Wu, C. Guo, L. Yu, P. Murto and X. Xu, *ACS Appl. Mater. Interfaces*, 2023, **15**, 10084–10097.

16 D. Ding, O. S. Rasmussen and M. Qin, *Energy Build.*, 2024, **313**, 114262.

17 T. T. Yang, K. R. Zhang, C. T. Mei, E. N. Ma and J. Z. Cao, *Wood Sci. Technol.*, 2022, **56**, 703–720.

18 T. T. Yang and E. Ma, *Int. J. Polym. Sci.*, 2016, 2454610.

19 O. F. Osanyintola and C. J. Simonson, *Energy Build.*, 2006, **38**, 1270–1282.

20 T. Alapieti, R. Mikkola, P. Pasanen and H. Salonen, *Eur. J. Wood Wood Prod.*, 2020, **78**, 617–634.

21 K. Nore, A. Q. Nyrud, D. Kraniotis, K. R. Skulberg, F. Englund and T. Aurlien, *Sci. Technol. Built Environ.*, 2017, **23**, 512–521.

22 M. Libralato, A. De Angelis, P. D'Agaro, G. Cortella, M. Qin and C. Rode, *J. Phys.: Conf. Ser.*, 2021, **2069**, 012043.

23 R. Sargent, *J. Wood Sci.*, 2019, **65**, 36.

24 K. Tu, X. Wang, L. Kong, H. Chang and J. Liu, *RSC Adv.*, 2016, **6**, 701–707.

25 K. Tu, X. Wang, L. Kong and H. Guan, *Mater. Des.*, 2018, **140**, 30–36.

26 C. Wang and C. Piao, *Wood Fiber Sci.*, 2011, 41–56.

27 Y. Ran, J. Li, S. Zhang, J. Wang, Y. Huang, W. Wang and J. Cao, *Chem. Eng. J.*, 2024, **488**, 150814.

28 Y. Ding, C. H. Dreimol, R. Zboray, K. K. Tu, S. Stucki, T. Keplinger, G. Panzarasa and I. Burgert, *Mater. Horiz.*, 2023, **10**, 257–267.

29 M. Ejeian and R. Z. Wang, *Joule*, 2021, **5**, 1678–1703.

30 N. Hanikel, M. S. Prévot and O. M. Yaghi, *Nat. Nanotechnol.*, 2020, **15**, 348–355.

31 G. Yilmaz, F. L. Meng, W. Lu, J. Abed, C. K. N. Peh, M. Gao, E. H. Sargent and G. W. Ho, *Sci. Adv.*, 2020, **6**, eabc8605.

32 M. W. Logan, S. Langevin and Z. Y. Xia, *Sci. Rep.*, 2020, **10**, 1492.

33 M. Qin, P. Hou, Z. Wu and J. Wang, *Build. Environ.*, 2020, **169**, 106581.

34 H. A. Almassad, R. I. Abaza, L. Siwwan, B. Al-Maythalony and K. E. Cordova, *Nat. Commun.*, 2022, **13**, 4873.

35 D. Ding, O. S. Rasmussen and M. Qin, *Build. Environ.*, 2024, **258**, 111581.

36 M. Qin, O. S. Rasmussen, J. Chen and L. Wadsö, *Build. Environ.*, 2024, 111757.

37 T. Liao, F. Luo, W. Liu, C. Ye, X. Liang, S. Wang, Z. Zhang, L. Wang and Y. Fang, *ACS Mater. Lett.*, 2024, **6**, 3462–3470.

38 L. Ge, Y. Feng, Y. Xue, Y. Dai, R. Wang and T. Ge, *Small Struct.*, 2023, **4**, 2300055.

39 K. Tu, B. Puértolas, M. Adobes-Vidal, Y. Wang, J. Sun, J. Traber, I. Burgert, J. Pérez-Ramírez and T. Keplinger, *Adv. Sci.*, 2020, **7**, 1902897.

40 K. Tu, S. Büchele, S. Mitchell, L. Stricker, C. Liu, C. Goldhahn, J. Allaz, Y. Ding, R. Günther and Z. Zhang, *ACS Appl. Mater. Interfaces*, 2022, **14**, 8417–8426.

41 R. Guo, X. Cai, H. Liu, Z. Yang, Y. Meng, F. Chen, Y. Li and B. Wang, *Environ. Sci. Technol.*, 2019, **53**, 2705–2712.

42 J. G. Sun, K. K. Tu, S. Buchele, S. M. Koch, Y. Ding, S. N. Ramakrishna, S. Stucki, H. Y. Guo, C. S. Wu, T. Keplinger, J. Perez-Ramirez, I. Burgert and G. Panzarasa, *Matter-Us*, 2021, **4**, 3049–3066.

43 A. Spiess, J. Wiebe, E. Iwaschko, D. Woschko and C. Janiak, *Mol. Syst. Des. Eng.*, 2022, **7**, 1682–1696.

44 Z. G. Wang, F. Y. Yin, X. F. Zhang, T. R. Zheng and J. F. Yao, *Sep. Purif. Technol.*, 2022, **293**, 121095.

45 Y. Gu, Y. C. Wang, H. M. Li, W. X. Qin, H. M. Zhang, G. Z. Wang, Y. X. Zhang and H. J. Zhao, *Chem. Eng. J.*, 2020, **387**, 124141.

46 X. Y. Zhu, M. J. Li, X. F. Zhang and J. F. Yao, *Microporous Mesoporous Mater.*, 2022, **342**, 112124.

47 S. N. Wang, C. Wang and Q. Zhou, *ACS Appl. Mater. Interfaces*, 2021, **13**, 29949–29959.

48 X. Y. Zhu, Z. X. Fan, X. F. Zhang and J. F. Yao, *J. Colloid Interface Sci.*, 2023, **629**, 182–188.

49 S. Roy, F. A. Philip, E. F. Oliveira, G. Singh, S. Joseph, R. M. Yadav, A. Adumbumkulath, S. Hassan, A. Khater and X. Wu, *Cell Rep. Phys. Sci.*, 2023, **4**, 101269.

50 Z. Wang, Y. He, L. Zhu, L. Zhang, B. Liu, Y. K. Zhang and T. Duan, *Mater. Chem. Phys.*, 2021, **258**, 123964.

51 G. Zhu, C. Zhang, K. Li, X. Xi, X. Zhang and H. Lei, *J. Porous Mater.*, 2023, **30**, 1171–1182.

52 R. G. AbdulHalim, P. M. Bhatt, Y. Belmabkhout, A. Shkurenko, K. Adil, L. J. Barbour and M. Eddaoudi, *J. Am. Chem. Soc.*, 2017, **139**, 10715–10722.

53 J. W. Zhang, P. Li, X. N. Zhang, X. J. Ma and B. Wang, *ACS Appl. Mater. Interfaces*, 2020, **12**, 46057–46064.

54 N.-X. Zhu, Z.-W. Wei, C.-X. Chen, X.-H. Xiong, Y.-Y. Xiong, Z. Zeng, W. Wang, J.-J. Jiang, Y.-N. Fan and C.-Y. Su, *Angew. Chem., Int. Ed.*, 2022, **61**, e202112097.

55 B. Lerma-Berlanga, C. R. Ganivet, N. Almora-Barrios, S. Tatay, Y. Peng, J. Albero, O. Fabelo, J. Gonzalez-Platas, H. Garcia, N. M. Padial and C. Marti-Gastaldo, *J. Am. Chem. Soc.*, 2021, **143**, 1798–1806.

56 A. J. Rieth, A. M. Wright, S. Rao, H. Kim, A. D. LaPotin, E. N. Wang and M. Dinca, *J. Am. Chem. Soc.*, 2018, **140**, 17591–17596.

57 H. Furukawa, F. Gandara, Y. B. Zhang, J. C. Jiang, W. L. Queen, M. R. Hudson and O. M. Yaghi, *J. Am. Chem. Soc.*, 2014, **136**, 4369–4381.

58 D. Ma, P. Li, X. Y. Duan, J. Z. Li, P. P. Shao, Z. L. Lang, L. X. Bao, Y. Y. Zhang, Z. G. Lin and B. Wang, *Angew. Chem., Int. Ed.*, 2020, **59**, 3905–3909.

59 Z. J. Chen, P. H. Li, X. Zhang, P. Li, M. C. Wasson, T. Islamoglu, J. F. Stoddart and O. K. Farha, *J. Am. Chem. Soc.*, 2019, **141**, 2900–2905.

60 N. M. Padial, E. Q. Procopio, C. Montoro, E. Lopez, J. E. Oltra, V. Colombo, A. Maspero, N. Masciocchi, S. Galli, I. Senkovska, S. Kaskel, E. Barea and J. A. R. Navarro, *Angew. Chem., Int. Ed.*, 2013, **52**, 8290–8294.

61 C. D. Hatch, J. S. Wiese, C. C. Crane, K. J. Harris, H. G. Kloss and J. Baltrusaitis, *Langmuir*, 2012, **28**, 1790–1803.

62 S. Wuttke, A. Zimpel, T. Bein, S. Braig, K. Stoiber, A. Vollmar, D. Müller, K. Haastert-Talini, J. Schaeske and M. Stiesch, *Adv. Healthcare Mater.*, 2017, **6**, 1600818.

63 C.-H. Liu, H.-C. Chiu, H.-L. Sung, J.-Y. Yeh, K. C.-W. Wu and S.-H. Liu, *Regul. Toxicol. Pharmacol.*, 2019, **107**, 104426.

64 R. R. Tian, C. Y. Duan, Y. Feng, M. J. Cao and J. F. Yao, *Energy Fuels*, 2021, **35**, 4604–4608.

65 H. F. Qin, Y. Zhou, Q. Y. Huang, Z. Yang, R. Y. Dong, L. Li, J. H. Tang, C. Y. Zhang and F. Jiang, *ACS Appl. Mater. Interfaces*, 2021, **13**, 5460–5468.

66 X. F. Zhang, Z. G. Wang, L. Song and J. F. Yao, *Sep. Purif. Technol.*, 2021, **266**, 118527.

67 J. L. Nguyen, J. Schwartz and D. W. Dockery, *Indoor Air*, 2014, **24**, 103–112.

68 M. Yang and H. Lei, *E3S Web Conf.*, 2022, **356**, 03037.

69 K. Lee and D. Lee, *Energy Procedia*, 2015, **78**, 2851–2856.

70 J. F. Yang, Q. Zhao, J. P. Li and J. X. Dong, *Microporous Mesoporous Mater.*, 2010, **130**, 174–179.

71 D. Y. Hong, Y. K. Hwang, C. Serre, G. Ferey and J. S. Chang, *Adv. Funct. Mater.*, 2009, **19**, 1537–1552.

72 Z. Zhang, M. Thiery and V. Baroghel-Bouny, *Cem. Concr. Res.*, 2016, **89**, 257–268.

73 B. Time, *Hygroscopic moisture transport in wood*, Norwegian University of Science and Technology, Trondheim, 1998.

74 Z. Zhang and U. M. Angst, *Drying Technol.*, 2022, **40**, 2741–2758.